CORRECTION OF ATMOSPHERIC AND BIDIRECTIONAL EFFECTS IN MULTISPECTRAL ADS40 IMAGES FOR MAPPING PURPOSES

U. Beisl[a, *], N. Woodhouse[b]

[a] Leica Geosystems GIS & Mapping GmbH, Heinrich-Wild-Strasse, CH-9435 Heerbrugg, Switzerland
Ulrich.Beisl@gis.leica-geosystems.com
[b] Leica Geosystems GIS & Mapping LLC, 10840 Thornmint Road, Suite 100, San Diego, CA 92127, USA
Neil.Woodhouse@gis.leica-geosystems.com

Commission VII, WG VII/1

KEY WORDS: Atmosphere, Mapping, Correction, Algorithms, Automation, Model, Mosaic, Sensor

ABSTRACT:

The radiometry of photogrammetric images is influenced by various effects from outside the camera. One prominent effect is the additional path radiance from atmospherically scattered sun light. This occurs especially at short wavelengths and long atmospherical path lengths, which gives rise to an increasing blueshift towards the borders of the images. Another effect is the bidirectional reflectance from the ground surface (BRDF). This effect depends on the illumination and the viewing geometry as well as on the wavelength and is caused by a varying amount of subpixel shadows on the ground. At high solar elevation, frame sensors encounter a bright area within the image, the so-called hot spot; line scanners like the ADS40 show an across-track brightness gradient. This prevents precise intra- and intercomparison of images, affects spectral ratios and is adverse to proper mosaicking. In order to correct the blueshift in the images a dark pixel subtraction algorithm is applied to the data, which accounts for the largest effects of the atmosphere. The algorithm takes into account the view angle dependence of the path radiance by calculating column statistics. For the bidirectional effect an automated semi-empirical algorithm is presented to correct a set of line scanner images simultaneously to a defined viewing and solar geometry. Statistics of the image brightness are calculated and the model fitted to the averages. These statistics can be calculated either from all pixels or can be class specific. The method is applied to ADS40 data after system and atmospheric correction in order to produce a well-defined input for the orthorectification and mosaicking. As an example, images from a flight campaign are processed to orthophotos and mosaicked without further dodging or feathering.

1. INTRODUCTION

"In most cases, the atmosphere is perceived as a hostile entity whose adverse impacts must be neutralized or eliminated before remotely sensed data can be properly analyzed." (Schott, 1997)
Despite the fact that atmospheric effects reveal physical properties of the atmosphere, this is usually not the aim of taking images.
Almost the same is true for bidirectional effects.
"The non-Lambertian nature of the terrestrial surface is a major source of unexplained variability in wide-swath satellite sensor data acquired in the solar reflective wavelength, hindering quantitative analysis in the spectral, temporal, and locational domains." (Chopping, 2000)
The bidirectional effects contain information about the geometric and biophysical structure of the object, which is a fascinating field of research, albeit progress is slow in developing universal models and model inversion techniques.
Applications of this research area range from new classification methods to crop yield predictions.
But again, this is usually not the intention of mapping imagery.
Therefore, fast empirical models which remove those effects are sufficient.

2. ATMOSPHERIC EFFECTS

The most prominent atmospheric effects in aerial images even under clear sky conditions are a general brightening and a blue hue which appears towards the borders of the images (i.e. for large view zenith angles. For a definition of the angles see Figure 1).

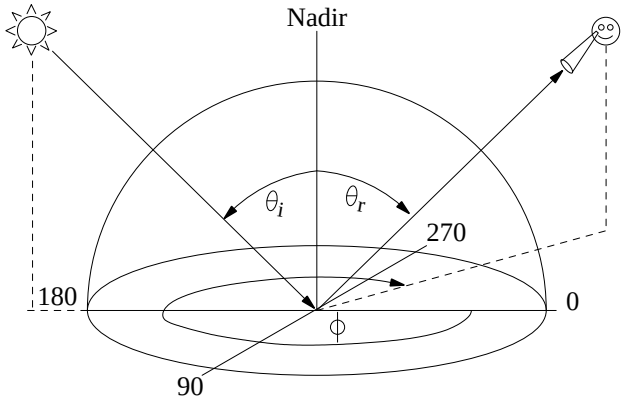

Figure 1. Coordinate system for reflection (θ_i incident solar zenith angle, θ_r reflected view zenith angle, φ view azimuth angle).

For operational purposes (no pressure cabin in plane) flight elevations below 4000 m (12.000 ft) are preferred. This reduces the amount of atmosphere between sensor and ground compared to satellite systems. However, in order to cover a reasonable

* Corresponding author.

ground area a field-of-view (FOV) of ±30 degrees and more is needed. Atmospheric absorption and scattering is highly angle dependent and so the atmospheric impact will be different within the image. This is true for framing cameras (classical aerial imaging cameras) or line scanner systems (like the ADS40). The appearance of the effect depends on the imaging principle: In framing cameras the atmospheric effects have a circular shape, while those in line scanner images have a linear shape. Usually linear shapes appear more disturbing, but this is a fact of human perception.
The atmospheric effects originate in gaseous absorption of the directly transmitted light and the gaseous (Rayleigh-) and aerosol (Mie-) scattering of indirect components reaching the sensor (Figure 2).

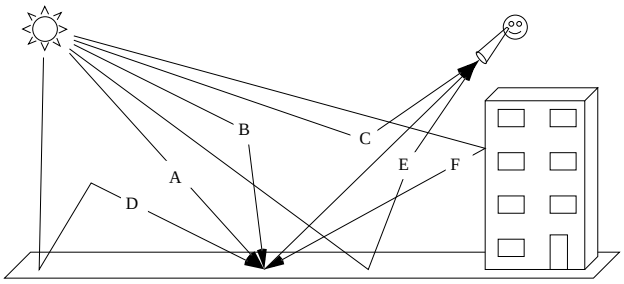

Figure 2. Radiation components reaching the sensor in the reflective wavelength range (400 nm – 2500 nm).

In classical aerial imaging cameras atmospheric effects have been thwarted by coloured gradient filters at the time of image capture. The atmospheric conditions had to be anticipated and no afterwards correction was possible. The path scattered upwelled radiance (path radiance, cf. Figure 2, component C) can be equal to the direct radiance for dark targets (1 to 3 % reflectance) (Schott, 1997, p. 118). This causes a general brightening of the image and reduces the contrast.
Nowadays with digitized aerial images and especially with digital cameras like the ADS40, atmospheric correction becomes an issue of post-processing. The difficult and time consuming task of removing the path radiance can be shifted to offline work.
Exploiting the higher pixel dynamics of digital cameras will reduce the need for higher resolution as suggested by the General Image Quality Equation GIQE (Leachtenauer et al., 1997): A doubling of the normalized relative edge response RER which is related to the contrast, can compensate for double the ground sampling distance GSD.

Satellite imagery, which is inherently digital, has initiated the development of a variety of procedures to convert sensor digital numbers (DN) to reflectance, a target property (the ratio of reflected to incoming light).

The process of generating reflectance images involves several steps:

1. Radiometric calibration: Convert DN to at-sensor radiances, a radiometric quantity measured in $W/m^2/sr/nm$.
2. Atmospheric correction: removal of the path radiance, i.e. the stray light from the atmosphere. Correction of the adjacency effect, the outshining of the target by nearby bright objects (Dave, 1980), cf. Figure 2, component E.
3. Correction of the anisotropic reflection properties of the targets (cf. sec. 3).
4. Reflectance calibration: removal of the spectral effect of solar illumination by dividing through the incoming irradiation.

Methods for reflectance image generation range from purely empirical methods to complex radiative transfer models. A more detailed discussion can be found elsewhere (Roberts et al., 1986, Moran et al., 1992). Simple methods try to cover the above sequence in one step, more accurate methods will do the steps individually.

The empirical methods can be divided into interactive methods where certain test areas have to be identified, like the “flat field” and the “empirical line fit” method (the latter requiring ground spectra) (Kruse, 1988).
Non-interactive empirical methods use statistical methods like the “dark-object subtraction” method (Chavez, 1975, and an improved version, Chavez, 1988).

Physically based methods, like ATCOR (Richter, 1996, Richter, 2002), ATREM/TAFKAA (Gao and Davis, 1997, Gao et al., 2000), ENVI/FLAASH (Research Systems, Inc.), or ACORN (Analytical Imaging and Geophysics, LLC), will use radiative transfer (RT) models, like the 6S model (Vermote et al., 1997) or MODTRAN (Berk et al., 1998).

Radiative transfer models require the knowledge of a set of parameters (atmosphere type/concentration profiles of gases, aerosol type and concentration, flight and ground elevation, illumination and view angles). Whereas the geometric parameters can be determined from flight management data, the atmospheric parameters are not immediately accessible to the user. In the case of imaging spectrometer data with adequate spectral channels, aerosol and water vapour concentration may be estimated from the data itself. However, this is not possible for the broadband channels of the ADS40.
Furthermore RT models tend to be time consuming and need optimization steps to be runtime efficient.

So according to the needs of different users, different strategies have to be taken for providing ADS40 reflectance images (Table 1).

User	Photogrammetry	Remote Sensing
Amount of data	Large	Usually limited
Processing speed	High	Moderate
Geometric accuracy	High	Moderate to low
Radiometric accuracy	Low	High
In-scene radiometric homogeneity	Moderate	High
Atmospheric correction	Empirical	Physical
BRDF correction	Empirical	Empirical or physical

Table 1. Requirements for radiometric data processing for photogrammetry and remote sensing.

3. BIDIRECTIONAL EFFECTS

Bidirectional effects have an impact on image quality of the same order of magnitude as atmospheric effects.
The most prominent effect is the so-called hot-spot in aerial images. It is placed at the projected solar position, opposite the

specular reflection position, and consists of a bright, shadow-free circular zone. For nadir images it appears always, when the solar zenith angle (= 90° - solar elevation) is smaller than the FOV of the camera.
For the ADS40 line scanner, the hot spot appears only in the case that both the solar zenith and azimuth angle match one of the CCD line viewing directions. Then the hot spot appears as a bright linear strip along the flight line. As with aerial images, the FOV of the ADS40 is an upper boundary for the solar zenith angle where a hot spot can occur, and even then it can easily be bypassed by avoiding certain times or flight directions.
Apart from the hot spot, the BRDF-effect will cause circular brightness gradients in aerial images and across-track gradients in line scanner images.

The origin of the bidirectional effects is mainly microscopic shadow casting (cf. Figure 3): Each image pixel consists of a mixture of pure or mixed material and cast shadow. This mixing goes from the scale of the pixel size down to the wavelength of light. Hence we will call it microscopic shadow here, because it is not visible at this resolution. The amount of cast shadow increases with increasing solar zenith angle (i.e. at dusk and dawn). The amount of microscopic cast shadow contributing to the pixel also depends on the viewers position: In the case of the hot spot, with the Sun in the back of the viewer, the cast shadow is hidden by the object itself, while with the Sun in the opposite direction the shadow is darkening the pixel (assuming no specular reflection). This shadow casting effect is often referred to as “geometric” or “surface” scattering.

A second source of bidirectional effects is multiple scattering between the structure elements of the target area, the so-called “volume scattering”. This is especially occurring in vegetation canopies.

Since the amount and the angular distribution of the bidirectional effect depends on the microscopic shape and structure of the target, it is possible to extract structural information of the ground from BRDF affected images.

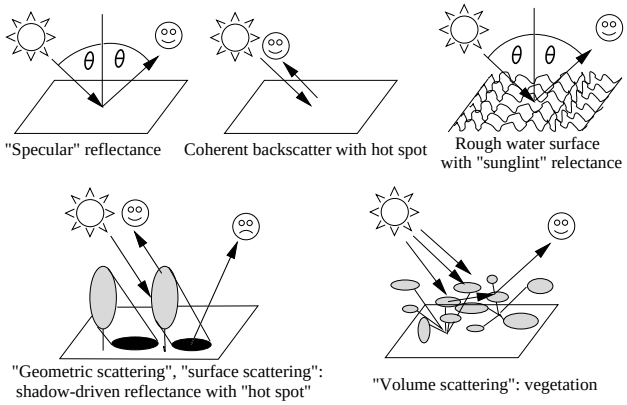

Figure 3. Sources of anisotropic reflectance from natural surfaces.

Many models, empirical and physically based, have been developed during the past forty years. Again, the inversion of physical models tends to be slow and may be unstable. But unless the bidirectional information itself is the goal, then the accuracy of empirical models is sufficient.

Linear semi-empirical models are fast and easy to invert (Chopping, 2000). They are a sum of so-called kernels, each of which is multiplied by a parameter. A widely used linear semi-empirical model is the Walthall model (Walthall, 1985), which contains 4 parameters in its extended version (Nilson and Kuusk, 1989), cf. Eqn 1.

$$\rho(\theta_i,\theta_r,\varphi) = a\theta_i^2\theta_r^2 + b(\theta_i^2+\theta_r^2) + c\theta_i\theta_r\cos\varphi + d \quad (1)$$

where ρ = reflectance factor
θ_i = incident illumination zenith angle
θ_r = reflection view zenith angle
φ = relative azimuth angle
a, b, c, d = free parameters

Unfortunately the Walthall model does not include a hot spot term. But by introducing an additional parameter, a hot spot term can be included. For simplicity we will use as an additional kernel the hot spot distance function of the Li-kernels from the AMBRALS model (Wanner et al., 1995), cf. Eqn 2.

$$D = \sqrt{\tan^2\theta_i + \tan^2\theta_r - 2\tan\theta_i\tan\theta_r\cos\varphi} \quad (2)$$

The samples for model inversion can be retrieved by calculating column averages of the total image as described in (Beisl, 2001), since a column in a line scanner image represents a line of constant view angle (cf. Figure 4). The relative shape of the modelling in then used for a multiplicative correction.
For a more accurate correction this statistics can be calculated for separate classes within the image. For a good inversion quality, i.e. for all images matching together in the mosaic, it is recommended to merge the statistics from each image together and perform a simultaneous correction (Beisl, 2002).

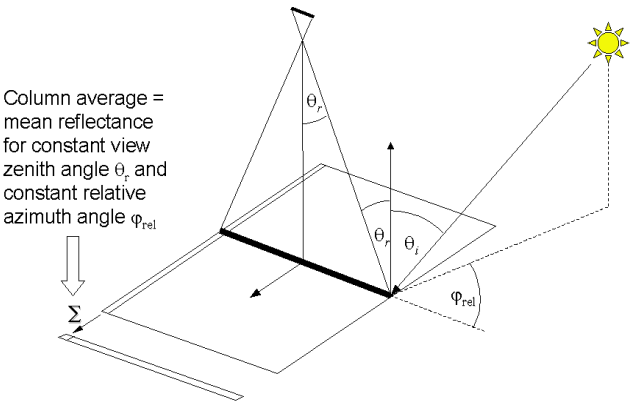

Figure 4. View and illumination geometry for a line scanner.

4. DATA AND RESULTS

As an example, data from a flight campaign in 2003 in Hinwil, Switzerland are shown (cf. Figure 5, Figure 6). Each image is a mosaic of an image strip merged with the image strip flown in the opposite direction. The merge is done by taking one square from one image and the subsequent square from the other image, in order to obtain a chessboard like mosaic. So wherever there is a difference between the images, a chessboard pattern will appear.

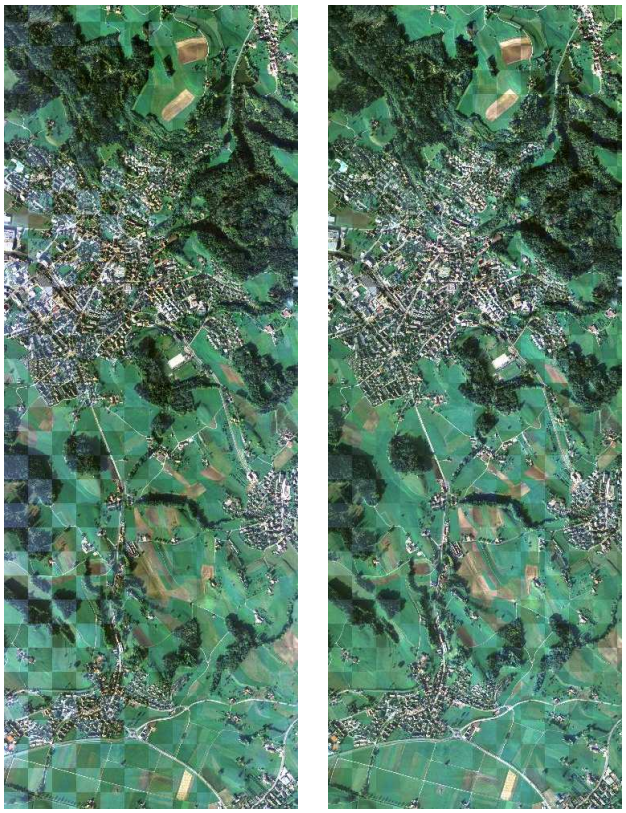

Figure 5. Image mosaics before (left) and after (right) BDRF correction. The mosaics each consist of two images flown in opposite direction (NS and SN) with the forward looking RGB lines of an ADS40.

Figure 6. Image mosaics before (top) and after (bottom) BDRF correction. The mosaics each consist of two images flown in opposite direction (EW and WE) with the forward looking RGB lines of an ADS40. Dark forest shows a larger discrepancy after correction and should be modelled separately.

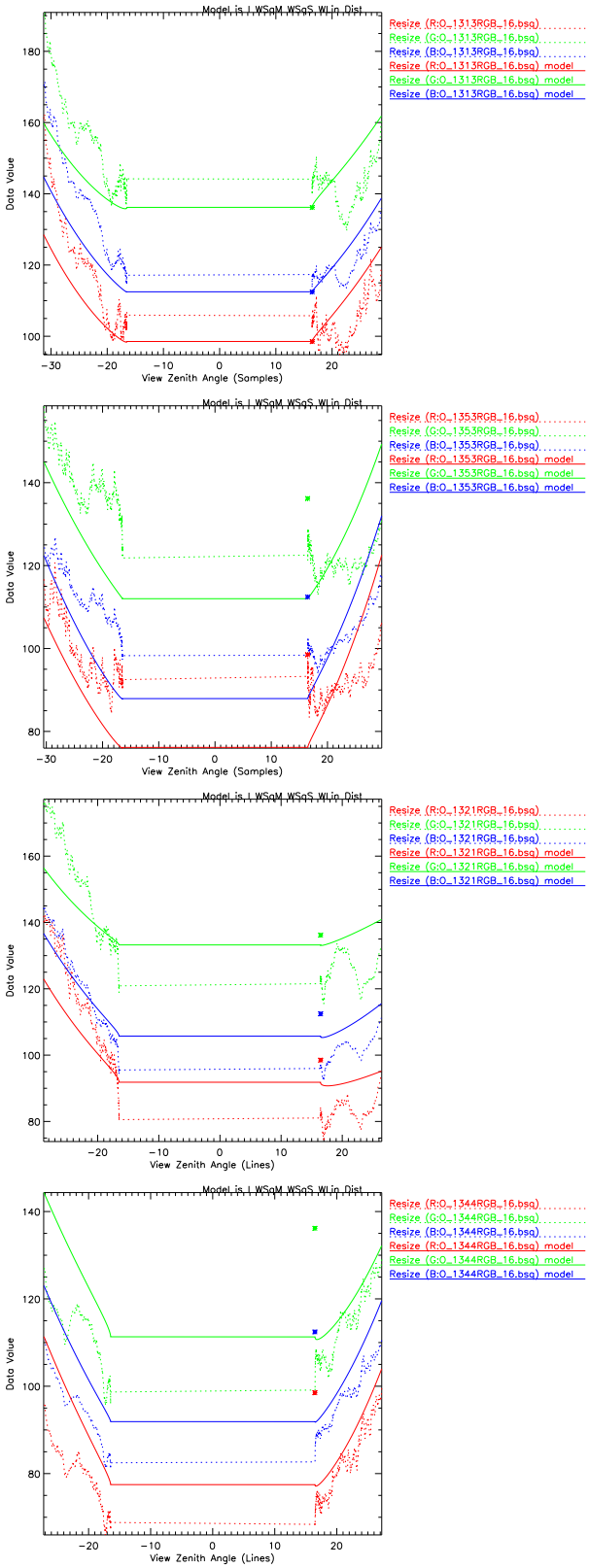

Figure 7. Column statistics (dotted lines) for the RGB bands of the NS, SN, WE, and EW flight line. The solid line is the modelling for the actual geometry and the asterisk denotes the view angle and brightness level of the final viewing geometry.

Since the two strips are taken with 20, resp. 40 minutes distance the solar position has moved. More important is the fact that the azimuth has turned by 180 degrees and that the RGB lines in this camera are looking 16 degrees forward. So even for the center pixels the viewing geometry has changed.

This can be clearly seen in the original data. When using the method described in sec. 3 a considerable reduction can be obtained.

The corresponding column statistics is shown in Figure 7. The statistics has got a gap between minus and plus 16 degrees because of the tilt angle of the RGB lines, which sets a minimum for the viewing angle (However, the ADS40 is also available with the RGB lines placed in Nadir position).

The modelling is sometimes off the data due to the nature of the model. However the relative shape is always maintained. It can be seen that the data have quite considerable differences in brightness level. The asterisk denotes the final view angle and brightness level (here the NS line) for which the correction will be performed. If the hot spot function is replaced by the Li Sparse Reciprocal MODIS kernel from the AMBRALS model the modelling quality is not significantly changed.

5. CONCLUSIONS

In this paper we have shown a strategy for correction of atmospheric and BRDF effects in ADS40 images.
The requirements for mapping imagery differ from those in remote sensing applications. The huge data amounts require fast and robust algorithms which produce seamless image mosaics. So empirical methods are the first choice unless the data quality requires higher accuracy.
For the case of the atmospheric correction this results in using an improved dark pixel method. The BRDF correction is performed using an improved Walthall model.
It was shown with ADS40 RGB image data that the brightness gradient could be removed and image brightness of different flight lines could be adjusted to match properly, without removing image fluctuations. Remaining seams can be removed with conventional feathering.
This is a step towards an automatic generation of huge seamless maps.

6. REFERENCES

Beisl, U., 2001. New method for correction of bidirectional effects in hyperspectral images. *Proc. 8th International Symposium in Remote sensing (SPIE)*, Toulouse, France.

Beisl, U., 2002. Simultaneous correction of bidirectional effects in line scanner images of rural areas. *Proc. 9th International Symposium in Remote sensing (SPIE)*, Agia Pelagia, Crete.

Berk, A., Bernstein, L. S., Anderson, G.P., Acharya, P. K., Robertson, D.C., Chetwynd, J. H., and Adler-Golden, S. M., 1998. MODTRAN cloud and multiple scattering upgrades with application to AVIRIS. *Remote Sens. Environ.*, 65, pp. 367-375.

Chavez, P. S., Jr., 1975. Atmospheric, solar, and MTF corrections for ERTS digital imagery. *Proc. Am. Soc. Photogrammetry*, Fall Technical Meeting, Phoenix, AZ, p. 69.

Chavez, P. S., Jr., 1988. An improved dark-object subtraction technique for atmospheric scattering correction of multispectral data. *Remote Sens. Environ.*, 24, pp. 459-479.

Chopping, M. J., 2000. Testing a LiSK BRDF model with in situ bidirectional reflectance factor measurements over semiarid grasslands. *Remote Sens. Environ.*, 74, pp. 287-312.

Dave, J. V., 1980. Effect of atmospheric conditions on remote sensing of a surface non-homogeneity. *Photogramm. Eng. Remote Sens.*, 46(9), pp. 1173-1180.

Gao, B.-C., Heidebrecht, K. B., and Goetz, A. F. H., 1993. Derivation of scaled surface reflectances from AVIRIS data. *Remote Sens. Environ.*, 44, pp. 145-163.

Leachtenauer, J. C., Malila, W., Irvine, J., Colburn, L., and Salvaggio, N., 1997. *Appl. Opt.*, 36(32), pp. 8322-8328.

Moran, S., Jackson, R. D., Slater, P. N., and Teillet, P. M., 1992. Evaluation of simplified procedures for retrieval of land surface reflectance factors from satellite sensor output. *Remote Sens. Environ.*, 41, pp. 169-184.

Nilson, T., and Kuusk, A., 1989. A reflectance model for the homogeneous plant canopy and its inversion. *Remote Sens. Environ.*, 27, pp. 157-167.

Richter, R., 1996. Atmospheric correction of DAIS hyperspectral image data. *Computers & Geosciences*, 22(7), pp.785-793.

Richter, R., and Schlaepfer, D., 2002. Geo-atmospheric processing of airborne imaging spectrometry data. Part 2: atmospheric/topographic correction. *Int. J. Remote Sensing*, 23, pp. 2631-2649.

Roberts, D. A., Yamaguchi, Y., and Lyon, R. J. P., 1986. Comparison of various techniques for calibration of AIS data. *Proc. 2nd Airborne Imaging Spectrometer Data Analysis Workshop*, JPL Publications, Pasadena, CA, pp. 21-30.

Schott, J. R., 1997. *Remote Sensing: The image chain approach.* Oxford University Press, New York.

Vermote, E.F., Tanré, D., Deuzé, J. L., Herman, M., and Mocrette, J.-J., 1997. Second Simulation of the Satellite Signal in the Solar Spectrum, 6S: An overview. *IEEE Transact. Geosci. Remote Sens.*, 35(3), pp. 675-686.

Walthall, C. L., Norman, J. M., Welles, J. M., Campbell, G., and Blad, B. L., 1985. Simple equation to approximate the bidirectional reflectance from vegetative canopies and bare soil surfaces. Appl. Opt., 24(3), pp. 383-387.

Wanner, W., Li, X., and Strahler, A. H., 1995. On the derivation of kernels for kernel-driven models of bidirectional reflectance. *J. Geophys. Res.*, 100(D10), pp. 21077-21089.

7. ACKNOWLEDGEMENTS

Many thanks to the ground spectrometry team of Dr. Kneubühler from the Remote Sensing Laboratories in Zurich who made accompanying BRDF measurements with the RSL Goniometer on the sand sports ground in Hinwil, Switzerland.